

Computational Fluid Dynamics in Hypersonic Aerothermodynamics

Krishnendu Sinha

Indian Institute of Technology Bombay, Mumbai-400 076
Email: krish@aero.iitb.ac.in

ABSTRACT

Hypersonic flows are characterised by high Mach number and high total enthalpy. An elevated temperature often results in thermo-chemical reactions in the gas, which play a major role in aerothermodynamic characterisation of high-speed aerospace vehicles. Hypersonic flows in propulsion components are usually turbulent, resulting in additional effects. Computational simulation of such flows, therefore, need to account for a range of physical phenomena. Further, the numerical challenges involved in resolving strong gradients and discontinuities add to the complexity of computational fluid dynamics (CFD) simulation. In this article, physical modelling and numerical methodology-related issues involved in hypersonic flow simulation are highlighted. State-of-the-art CFD challenges are discussed in the context of two prominent applications—the flow in a scramjet inlet and the flow field around a re-entry capsule.

Keywords: Hypersonic aerothermodynamics, computational fluid dynamics, scramjet engine, hypersonic flows, scramjet inlet, re-entry capsules

1. INTRODUCTION

Hypersonic flows are often defined in terms of Mach number exceeding 5. These high Mach number flows are characterised by strong shock waves and expansion waves. It is common to have multiple shock/expansion waves intersecting with each other, resulting in a complex flow pattern. Interaction of shock waves with the boundary layer on vehicle walls often results in local flow separation and reattachment. Separation bubbles act as a blockage to the flow, resulting in additional shock waves.

The high speed, and therefore, high total enthalpy of the gas encountered in a hypersonic flow is converted to internal energy across a shock wave. The post-shock temperature can be high enough to excite internal energy modes and initiate dissociation of gas molecules. The working medium can no longer be treated as a perfect gas, and the thermo-chemical relaxation processes in the gas have to be accounted for to predict its properties accurately.

Hypersonic flow applications span a wide range of free-stream densities—from rarefied conditions at the outer extremities of the atmosphere to continuum flow at lower altitudes. At relatively high Reynolds numbers, a part of the flow can be unsteady, transitional or turbulent. Presence of turbulent fluctuations brings in additional challenges and uncertainties in computing such flow fields. Presence of shock waves and their interaction with the turbulent fluctuations aggravates the situation. Numerical simulation of hypersonic flows need to account for the physics associated with the different phenomena outlined above. The physical models are at times based on approximations and limited

experimental data, which limit the accuracy of the computational fluid dynamics (CFD) predictions. In addition, the numerical error associated with resolving high gradients and discontinuities can lead to unphysical solutions. Both the numerical method and the computational grid play a significant role in bounding the error in the solution. Grid generation is even more important in real-life configurations, where the geometric complexity and the flow field gradients require extreme care to obtain good quality solution.

Hypersonic aerothermodynamics is critical to the design and operability of high-speed aerospace vehicles, both for military applications and for access to space. External aerodynamics of these vehicles are concerned with managing the high heating loads and maintaining adequate effectiveness of the control surfaces. On the propulsion side, optimum performance of inlet ducts and nozzles are determined mainly by the flow in these components. Computational fluid dynamics plays a major role in the design and development of hypersonic vehicles and their components. CFD prediction of peak heating load at re-entry is critical to the design of the thermal protection system. Performance parameters of hypersonic inlets obtained from CFD are invaluable in the overall feasibility of a scramjet engine. Computational fluid dynamics contribution is especially valuable because achieving hypersonic flight conditions in ground-based experimental facilities is either not feasible or prohibitively expensive. In addition, numerical simulation can provide a detailed understanding of the flow physics, which aids in designing better components or explore new ideas in flow control.

In this review, the different aspects of hypersonic CFD are discussed in the context of two applications: the flow in a scramjet inlet, and the flow around a re-entry capsule. Both applications are highly relevant in the present Indian context¹⁻⁵, as well as internationally.⁶⁻¹¹ These flows cover the entire range of physical phenomena outlined above, and their modelling in the CFD context is discussed in detail. They also bring out the CFD challenges involved in practical applications.

2. COMPUTATIONAL FLUID DYNAMICS OF SCRAMJET INLETS

The function of a scramjet inlet is to compress the air entering the engine, while encountering minimum losses and achieving close-to-uniform flow at combustor entry. The incoming air is compressed through a series of oblique shock waves. An associated rise in density in the inlet duct, and resulting high Reynolds number, makes the boundary layer on the wall turbulent. Interaction of the shock waves with the boundary layer often leads to local flow separation. The associated losses, flow blockage, and high heating can be detrimental to the performance of the inlet.

Numerical simulation of a scramjet inlet flow field solves the Reynolds-averaged Navier-Stokes equations¹². The turbulence models¹³⁻¹⁵ employed in these computations are mostly developed for low-speed applications. Compressibility corrections currently available are also not adequate to predict shock-dominated flows correctly. The CFD solutions of shock boundary layer interactions in scramjet inlets are often limited by their accuracy in predicting the extent of flow separation¹⁶. Recent efforts towards modelling of shock/turbulence interaction has quantified the limitations of the existing turbulence models. Advanced models are now available that improved CFD predictions significantly¹⁷.

2.1 Modelling of Shock/Turbulence Interaction

Majority of turbulence models used in practice are based on the Boussinesq approximation, which models Reynolds stresses τ_{ij} in terms of Eddy viscosity μ_T ¹²

$$\bar{\rho}\tau_{ij} = 2\mu_T S_{ij} - \frac{2}{3}\mu_T S_{kk}\delta_{ij} - \frac{2}{3}\rho k\delta_{ij} \quad (1)$$

where $\bar{\rho}$ is the mean density, $S_{ij} = (1/2)(u_{i,j} + u_{j,i})$ is the rate of strain tensor, and \bar{u}_i is the mean velocity component. μ_T is computed from turbulent quantities like the turbulent kinetic energy k and the turbulent dissipation rate ϵ . The transport equation for k in the k - ϵ turbulence model has source terms corresponding to production and dissipation mechanisms. The production term given by

$$P_k = \mu_T \left(2S_{ij}S_{ji} - \frac{2}{3}S_{ii}^2 \right) - \frac{2}{3}\bar{\rho}kS_{ii} \quad (2)$$

is active in a shock wave and assumes very high values. For example, in case of a normal shock

$$P_k = \mu_T \left(\frac{\partial u}{\partial x} \right)^2 \quad (3)$$

This results in unrealistically high values of k downstream the shock (Fig. 1). The standard k - ϵ model predicts very high amplification of turbulent kinetic energy. The amplification is reduced using realisable k - ϵ model and further using $\mu_T = 0$. The new model including shock-unsteadiness effect reproduces the correct level of turbulent kinetic energy downstream the shock¹⁷. The amplification of k increases rapidly as the grid is refined to get a thinner shock, leading to problems in grid convergence. It is argued¹⁷ that this non-physical effect is caused by the fact that the Eddy viscosity assumption breakdown in highly non-equilibrium flows like shock/turbulence interaction. Suppressing the eddy viscosity, for example, in a realisable k - ϵ turbulence model or by setting $\mu_T=0$, yields lower values of k -amplification (Fig. 1).

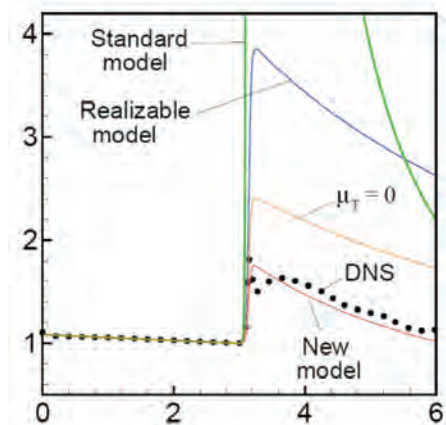


Figure 1. Evolution of k in the interaction of homogeneous isotropic turbulence with a normal shock (located at $X = 3.0$). Different variations of the k - ϵ model are compared with DNS data. Reproduced from Ref. 17.

The fundamental interaction of homogeneous isotropic turbulence with a normal shock is studied in detail¹⁷ and was found that eddy viscosity corrections of the form used in realisable models even in the limiting case of $\mu_T=0$, are not enough to match DNS data. A detailed study of the transport equation for k at the shock revealed a new physical mechanism due to unsteady shock motion that could explain the discrepancy between the model and the DNS. The turbulent fluctuations cause local distortion in an otherwise steady shock wave.

The unsteady shock motion gets coupled to the incoming velocity fluctuations, resulting in a negative source term in the k -equation. This damping mechanism was modelled using theoretical analysis. The production term in the new model has the form

$$P_k = -\frac{2}{3}\bar{\rho}kS_{ii}(1-b') \quad (4)$$

where $b' > 0$ is the shock-unsteadiness modeling parameter and is a function of the upstream Mach number normal to the shock. The new model was found to match DNS data^{17,18}(Fig. 1).

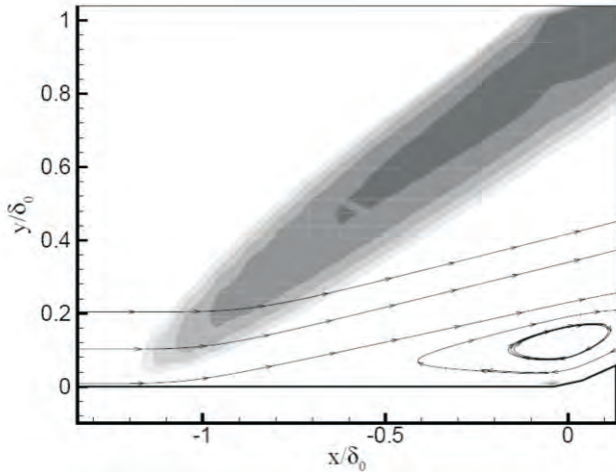


Figure 2. Magnified view of compression corner flow at Mach 2.84 and 24° ramp. The separation bubble is identified in terms of reversed flow streamlines and the separation shock corresponds to the grey region where S_{ii} is negative¹⁹. (Reprinted with permission of the American Institute of Aeronautics and Astronautics).

The shock unsteadiness correction is incorporated in standard $k-\epsilon$, $k-\omega$ and Spalart Allmaras models, and applied to canonical flows like a compression corner¹⁹. The test cases were selected such that detailed experimental data is available for turbulence model validation. The shock-unsteadiness correction is implemented in such a way that it is effective only in high compression regions of the flow, and the original model is recovered outside of shock waves. A negative value of S_{ii} was used to identify the shock waves in the flow (Fig. 2). The models including shock-unsteadiness correction move the separation point upstream as compared to the standard models. The location of the corresponding pressure rise (at $s/\delta_0 = -2$) matches better with experimental data (see Fig.3). Also in the case of an oblique shock impinging on turbulent boundary-layer, the shock unsteadiness modification increases the size of separation bubble, such that the shape and location of different shock waves match experimental results better than that of the standard model (Fig.4).

2.2 Real-life Application

The flow-fields generated on the forebody and intake duct of a scramjet engine (Fig. 5) are characterised by shock/turbulent interactions of the kind discussed before. For example, reflection of the cowl shock on the opposite wall often results in flow separation similar to that described in Fig. 4. Although the basic nature of the interaction is identical to the canonical case, geometric complexity in a realistic configuration makes the overall flow field more complex. Presence of an expansion corner upstream the cowl shock impingement location makes the shock wave stronger and alters the boundary layer on the bottom wall. Experimental data for

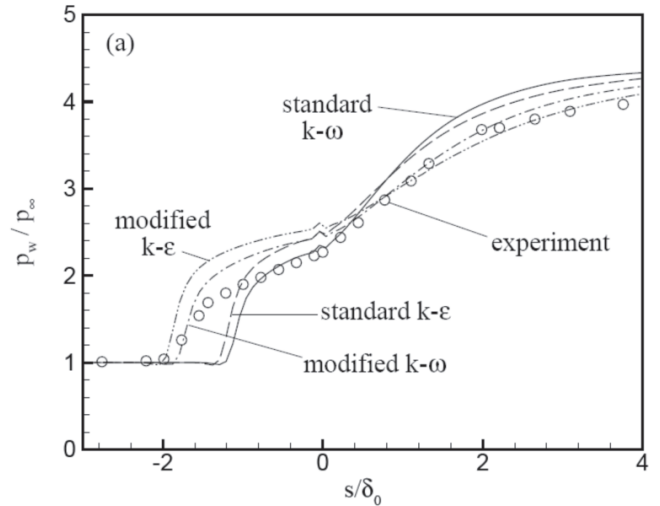


Figure 3. Variation of normalised surface pressure along a 24° compression corner obtained using different $k-\epsilon$ and $k-\omega$ models¹⁹. (Reprinted with permission of the American Institute of Aeronautics and Astronautics).

such configurations are often unavailable, and extensive CFD validation in canonical configurations of the kind¹⁹⁻²⁴ are helpful in predicting these flow fields reliably.

Three-dimensionality of a real life scramjet inlet geometry results in additional complexity in the flow pattern. The cowl shock interacts with the boundary layer on the side wall. This configuration is studied in literature as the single-fin geometry²⁵ where the fin acts as a shock generator and the boundary layer on the adjacent wall separates to form a conical region. The footprint of this helical flow

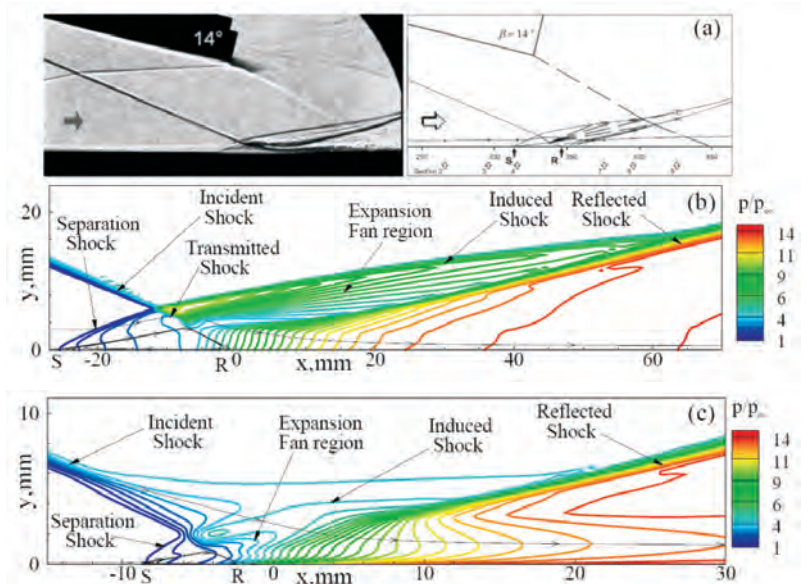


Figure 4. Oblique shock wave generated by a 14° wedge at Mach No. 5 impinging on a turbulent boundary layer: (a) experimental shadow graph, (b) computed pressure contours using the shock unsteadiness-modified $k-\omega$ model, and (c) standard $k-\omega$ model. (Figure reproduced from Ref. 20)

in terms of the surface streamlines is shown in Fig. 6, with the separation and reattachment lines identified. The planar inviscid shock bifurcates into a lambda structure near the side wall. The triple point formed at the junction of shock waves generates a jet like flow. Impingement of this supersonic jet on the wall leads to localised high pressure and heat transfer on the surface²⁶.

The actual flow in an inlet duct is a combination of the single-fin interaction on the side wall and an oblique shock impingement on the opposite ramp wall, as discussed before. The geometry shown in Fig. 7 was used to study a typical inlet flow field. The cowl is modelled as a 21° shock generator and the ramp surface is taken to be flat to avoid additional complexity due to the presence of an expansion corner. The shock pattern away from the side wall (Fig. 8) is similar to the 2-D result presented in Fig. 5. Impingement of the cowl shock on the ramp surface results in a large separation bubble, and several other shock waves and expansion fans are generated. However,

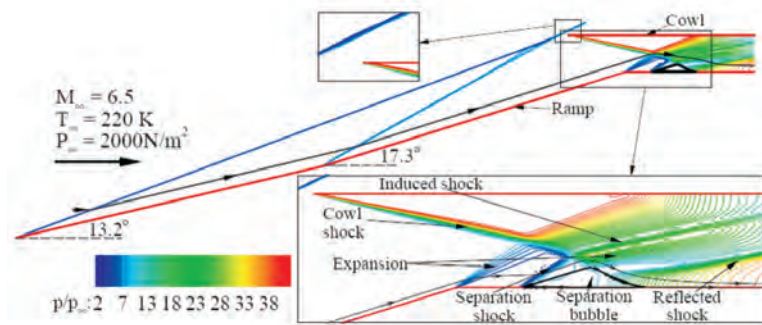


Figure 5. Shock structure in a simulated two-dimensional scramjet inlet geometry. The oblique shocks generated by the forebody ramps intersect slightly away from the cowl lip (inset). The cowl shock reflected from the opposite wall causes local flow separation and reattachment (inset).

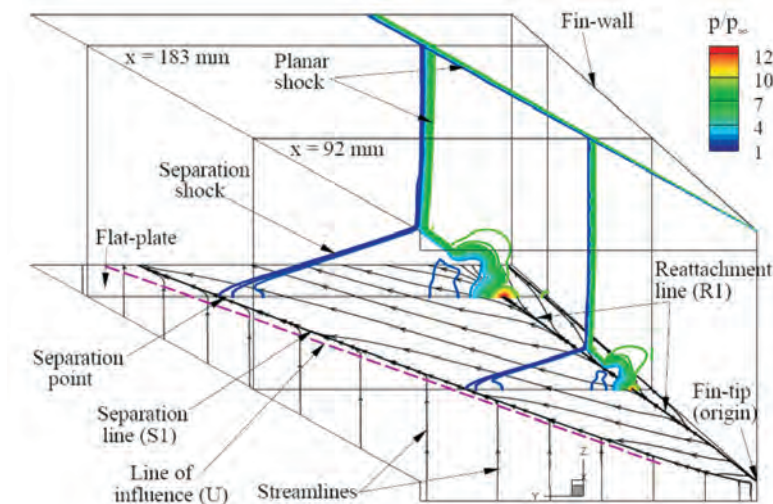


Figure 6. Shock structure in a simulated single fin shock/turbulent boundary layer interaction (shown by pressure contours in $x=92$ and 183 sections). Surface streamlines are plotted on the adjacent wall. (Figure reproduced from Ref. 21).

the shock waves got significantly distorted as these approached the side wall, with a lambda structure typical of single fin flow clearly visible in Fig. 9(a). Merging of the separation and cowl shock waves can be seen in Fig. 9(b) plotted further downstream. The surface stream lines plotted on the side wall show the conical single fin pattern, which gets altered by the flow separation on the opposite wall. Boundary layer flow separating from the side wall rolls up into a streamwise vortex (Fig. 10) that covers an appreciable portion of the inlet duct. The resulting flow distortion can have significant effect on the flow quality entering the combustor.

3. COMPUTATIONAL FLUID DYNAMICS OF RE-ENTRY CAPSULE

Re-entry capsules are blunt-bodies designed to withstand high heating loads experienced during entry into the atmosphere. Typically, these have a spherically-blunted nose and a tapered or flat afterbody. A bow shock forms ahead of the vehicle to slow down the hypersonic flow.

The Mach number in the shock layer is mostly subsonic. The flow expands around the shoulder to reach supersonic Mach numbers. The boundary layer that is formed on the forebody separates beyond the shoulder to form a large recirculation region, leading to the wake flow. The main features of a re-entry flow field are highlighted in Fig. 11 and the associated challenges for CFD are discussed.

The gas temperature in the shock layer reaches several thousands of degrees. At these temperatures, the internal energy modes of the gas molecules are excited. In a CFD simulation, the gas molecules are usually characterised by two temperatures – a translational-rotational temperature and a vibrational temperature²⁷. The relaxation process between the internal energy modes is accounted for by solving a separate equation for the vibrational energy²⁸. The chemical reactions are modelled by treating the working fluid as a mixture of perfect gases. For example, air is taken as a mixture of five species (N_2 , O_2 , NO , N , O) with five chemical reactions to account for dissociation/recombination effects²⁷. Higher number of species and reactions are considered to model ionisation effects in higher enthalpy flows²⁸⁻³¹.

The density of the gas varies over a large range in a re-entry flow field (Fig. 12), and it has an important effect on the state of thermo-chemical reactions in the gas. The density increases by an order of magnitude across the bow shock, and increases further in the vicinity of a cold wall. The increased density may equilibrate the thermo-chemistry in the gas. The fluid density decreases rapidly as the gas expands around the shoulder, to reach levels significantly lower than the free-stream value on the afterbody. This results in a frozen thermo-chemistry in the recirculation bubble. Thus, the flow field around a re-entry capsule may span all three regimes—equilibrium, nonequilibrium, and frozen—of thermo-chemistry, and a finite-rate thermo-

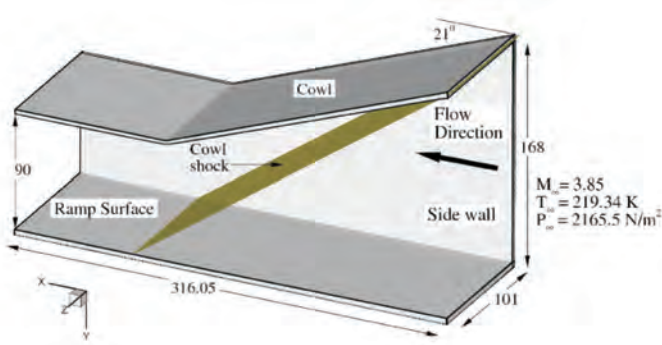


Figure 7. Simulated three-dimensional geometry of scramjet inlet duct to study the interaction of cowl shock with the side wall and the ramp surface.

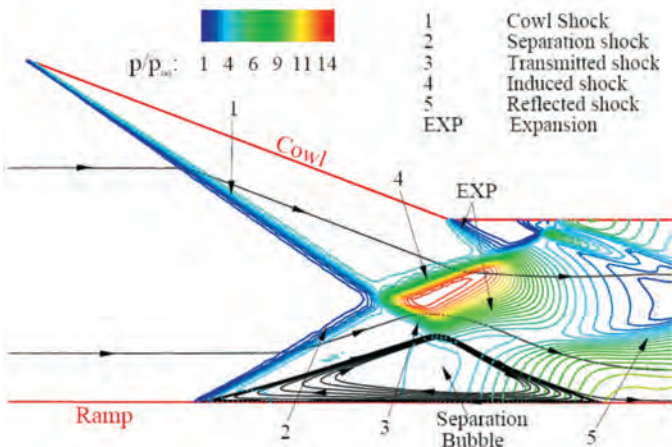


Figure 8. Pressure contours drawn in a stream-wise plane away from the side wall show a flow pattern similar to that in Fig. 7.

chemical model is required to accurately predict the gas composition. The properties of the working fluid, like viscosity and thermal conductivity, depend on the mixture composition.³² Several methods are available to compute the contribution of each species^{30, 33}. Local peaks at the expansion corners is noticed. Nose stagnation point heating rate matches with the theoretical estimate of Fay and Riddell correlation³⁴.

The hot gas enveloping the capsule results in high convective heat transfer to the vehicle walls (Fig. 13). Predicting the heat load is one of the most important contribution of CFD towards the design of the thermal protection system. A drop in temperature in the thermal boundary layer on the vehicle surface initiates recombination of atoms into molecules. The extent of these exothermic reactions in the near-wall region determines the gas temperature in the immediate vicinity of the wall. The mixture conductivity is also a strong function of its composition, which has additional bearing on the surface heat flux. Any uncertainty in the reaction rates therefore affects the heating rate predictions³⁵. The heat flux is also influenced by other factors like surface catalysis³⁶, transition, and turbulence. The strong shock wave, that forms ahead of the capsule, is prone to numerical errors, and a robust numerical method

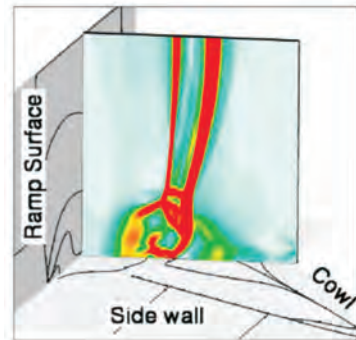
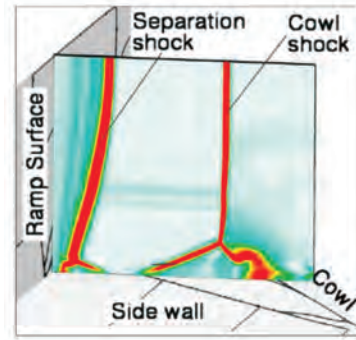


Figure 9. Shock structure in the vicinity of the side wall as shown by pitot pressure contours plotted in two transverse planes. The surface streamlines on the sidewall are also shown for reference.

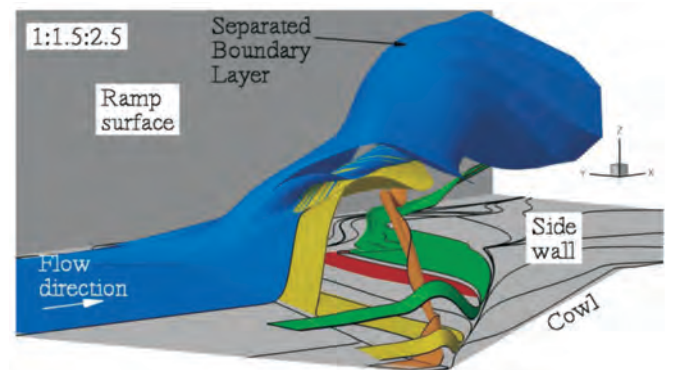


Figure 10. Three-dimensional separation of the side wall boundary layer due to interaction with the cowl shock, as shown in terms of different stream surfaces originating in the incoming boundary layer.

is required to capture it accurately. Finite volume methods based on flux-vector splitting³⁷ approach are commonly employed at hypersonic Mach numbers. Additionally, flux-limiters are required to avoid spurious oscillations at the shock. There are a wide variety of flux evaluation methods and limiters available in literature, and a comprehensive comparison is available in a hypersonic shock-shock interaction flow simulation is presented³⁸. Most of the state-of-the-art numerical methods capture the shock wave within two grid cells. A fine grid is therefore required in the vicinity of the shock wave to predict it accurately. In addition, one set of grid lines should be carefully aligned to the

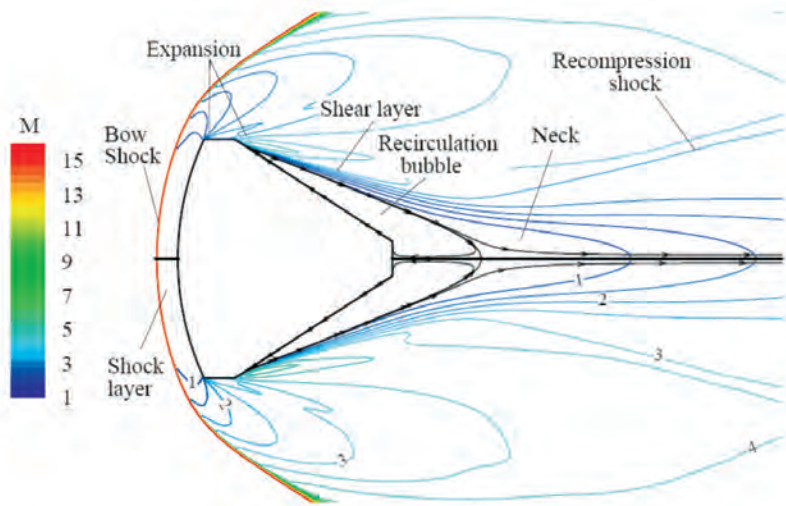


Figure 11. Mach number distribution in the flow around FIRE II re-entry capsule at Mach 16. Representative streamlines are shown on the afterbody to identify the re-circulation bubble.

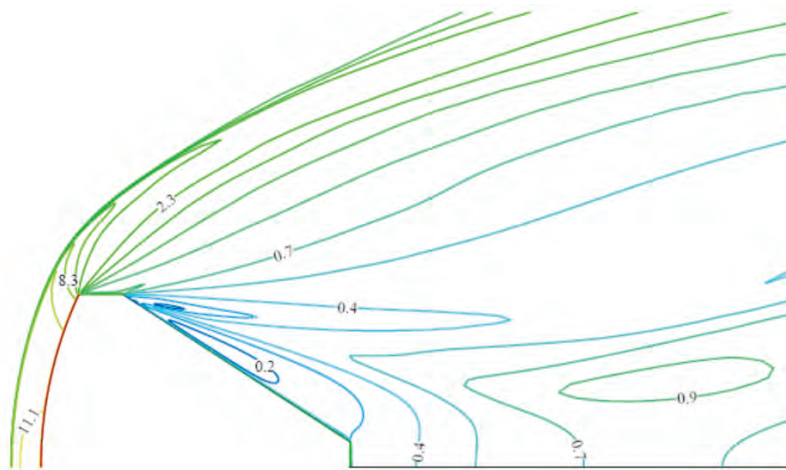


Figure 12. Distribution of the gas density, normalised by free-stream density, in the flow around a re-entry capsule at Mach 16.

shock wave. Even a small misalignment of the shock with the grid cell results in large variations in the stagnation point heat flux (Fig. 14). Algorithms are available to iteratively tailor the computational grid to the shock wave until a perfect alignment is obtained³⁹.

The highest heating loads are experienced on the forebody of a re-entry capsule. A drop in temperature, as the flow expands around the shoulder, results in much lower convective heat flux on the afterbody (Fig. 13(b)). However, boundary layer separation behind the vehicle makes it more challenging to compute the afterbody flow field accurately. The location of the separation point and free shear layer enclosing the separation bubble are sensitive to the computational grid, both to the grid point density and relative orientation between the flow gradients and the grid lines. A careful grid-refinement study, based on local refinement in the critical regions, may be required to build confidence on the computed results (Fig. 15).

The effect of angle of attack on a re-entry capsule flow field is shown in Fig. 16. The flow around the vehicle is symmetric at $\alpha = 0$. For non-zero angle of attack, the bow shock is asymmetric and the stagnation point shifts to the windward side. The wake is also highly skewed for $\alpha \neq 0$, with attached flow on the windward afterbody. The afterbody surface data plotted in Fig. 17 shows high heat flux at the base for the $\alpha = 0$ case. By comparison, no such hot region is present for the non-zero angle of attack. The limiting streamlines on the surface show a complex flow pattern for $\alpha \neq 0$ with the attached flow region having higher heat flux than the separation bubble.

The complexity of re-entry flow fields makes it essential that the computed solution be validated against theory or measurements. It is often difficult, if not impossible, to replicate flight conditions in terms of its Mach number, total enthalpy, and Reynolds

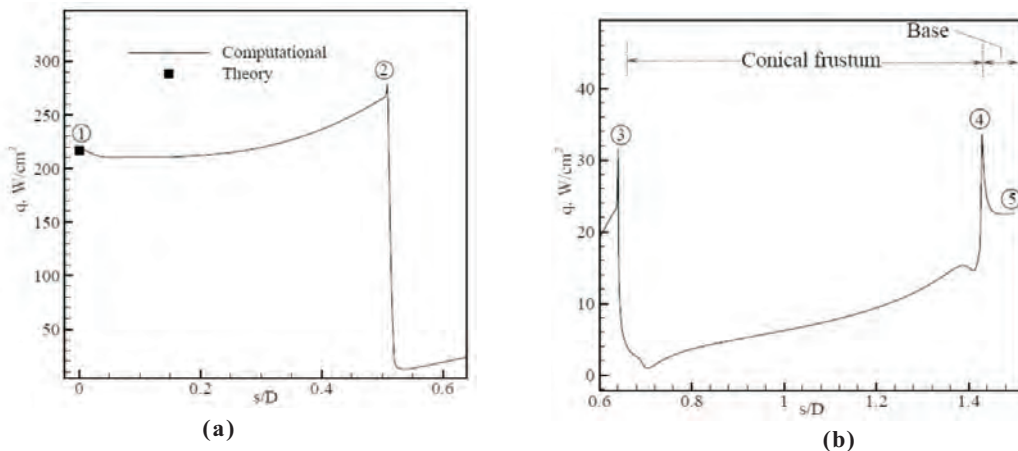


Figure 13. Surface heating rate obtained on FIRE II vehicle at Mach No. 16: (a) forebody, and (b) afterbody. s/D is the normalised arc length from the nose of the vehicle and the locations 1,2,3,4,5 corresponds to nose stagnation point, forebody shoulder, heat shield-backshell interface, after shoulder, and after stagnation point. (Reprinted with permission of the American Institute of Aeronautics and Astronautics).

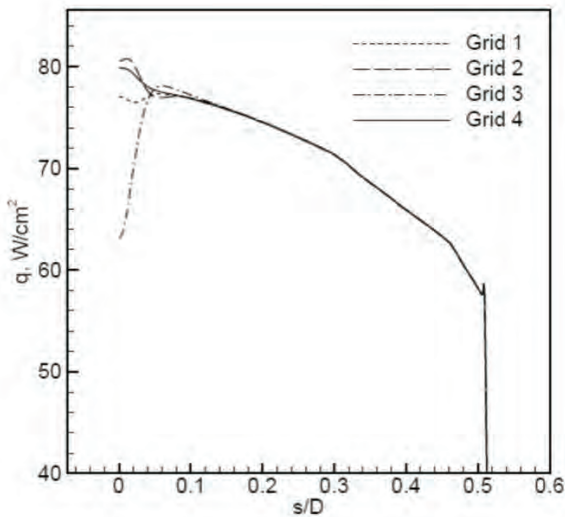


Figure 14. Effect of grid alignment to the shock wave on heat transfer rate at Mach No. 26.2 flow around a capsule at an altitude of 70 km. Highest sensitivity can be observed at the stagnation point ($s/D = 0$). The four grids are almost identical, with less than 1 per cent variation at the shock wave.

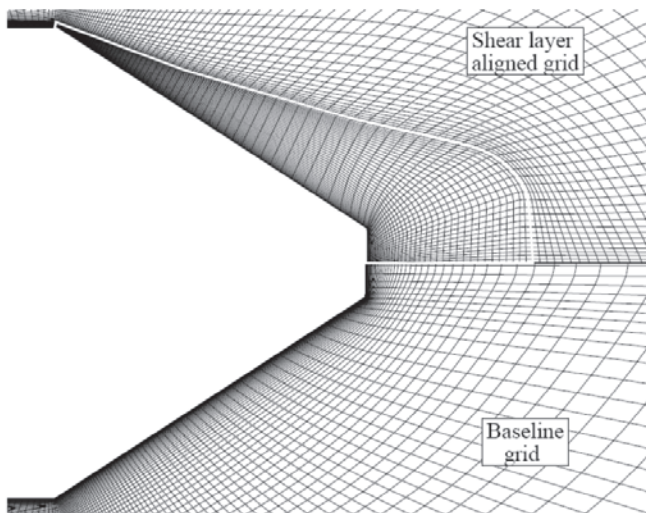


Figure 15. Afterbody grid for FIRE II vehicle simulations at Mach No. 16 and altitude of 35 km. Bottom half shows the baseline single block grid and the top half is a solution adapted grid that has a separate grid block for the recirculation bubble. The grid lines are aligned to the free shear layer to capture it accurately. White line indicates the block boundary.

number. Further most ground-based experimental measurements of afterbody heat flux are influenced by sting effects. It is therefore desirable to validate CFD predictions of afterbody flow field against in-flight measurements. Recent attempts in this direction have shown that it is possible to predict afterbody heating rate accurately in laminar³¹ and turbulent regimes²⁷, as well as for non-zero angle of attack⁴⁰. Computed afterbody heat transfer rate of FIRE II capsule at 35 km altitude is compared with in flight measurements⁴¹ in Fig. 18. Computations are performed with different turbulence models

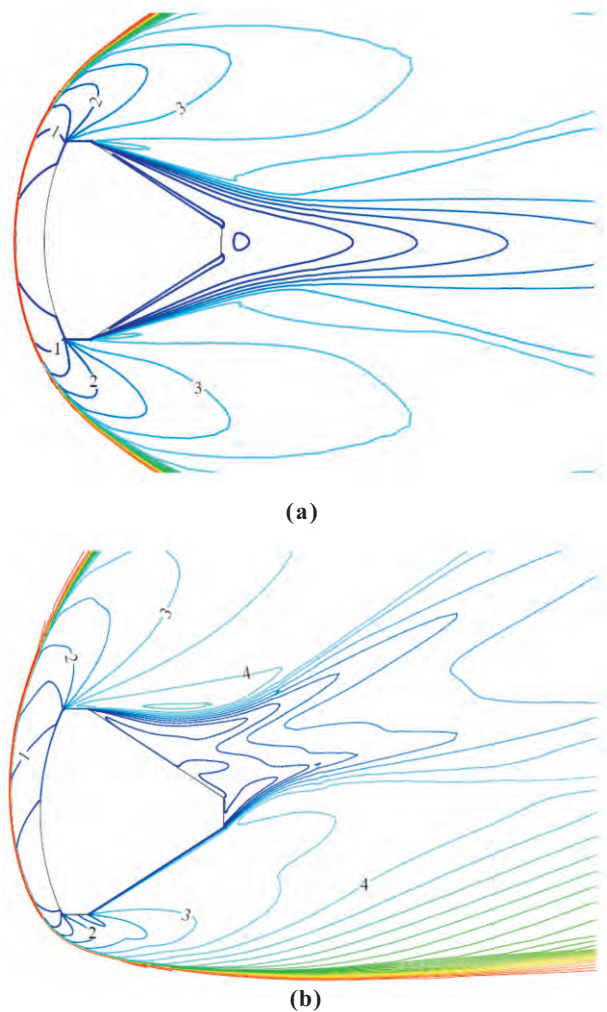


Figure 16. Distribution of Mach number on the pitch plane of a re-entry flow field at different angles of attack: (a) 0°, and (b) 20°.

and with laminar approximation. Heat flux is measured at four axial locations along three circumferential rays. The turbulent predictions compare well with the flight data whereas the laminar results are unsteady and much lower than measurements.

4. CONCLUSIONS

Computation of hypersonic flows needs to address challenges in physical modelling as well as issues related to the numerical methodology. The range of physical phenomena includes non-equilibrium thermo-chemistry in a high temperature gas to turbulent fluctuations at high Reynolds numbers. Numerical challenges are primarily associated with capturing high gradients and discontinuities. Geometric details of a real-life configuration and grid sensitivity of the numerical solution add to the complexity of the simulation. In this paper, state-of-the-art CFD methodology and its challenges are discussed for practical applications like scramjet inlets and re-entry capsules. The entire range of issues, from fundamental aspects of physical modelling to the challenges in real-life configurations, are addressed. Special emphasis is laid on a detailed understanding of the flow physics and

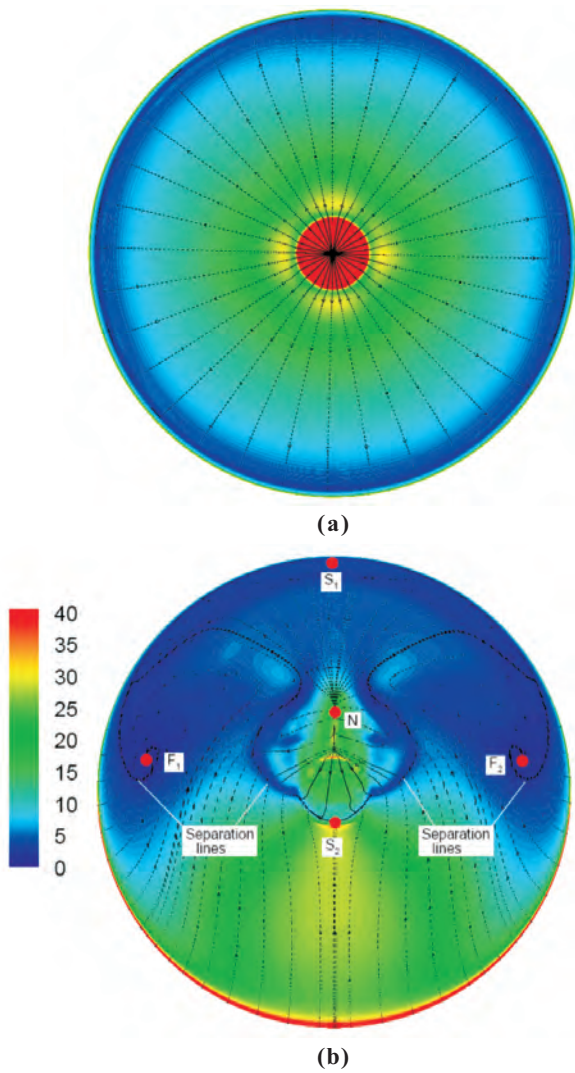


Figure 17. Surface streamlines and heat transfer rate on a re-entry capsule afterbody at different angles of attack: (a) zero degree, and (b) 20°. S_1 and S_2 are saddle points. F_1 , F_2 are foci, and N is a node. F and N can represent flow separation or re-attachment points on the wall, whereas S represents flow movement along the wall.

a careful validation of the CFD solution against experimental or in-flight measurements. Recent data shows that CFD based on appropriate physical models, a robust numerical technique, and careful grid refinement can accurately predict complex hypersonic flows in real-life configurations.

REFERENCES

1. Ganesh Anavaradham, T.K.; Thiagarajan, V. & Panneerselvam, S. Improvements in intake starting characterisation for a hypersonic cruise vehicle. *In Proceedings of the Symposium on Applied Aerodynamics and Design of Aerospace Vehicle (SAROD-2009)*, Bangaluru, India, 10-12 December 2009. 336-44.
2. Satyanarayana, A.; Ch. Srikanth; Chandra Sekhar, J. & Ramana, S.V. Experimental study on effect of cowl hinge location on starting characteristics of hypersonic

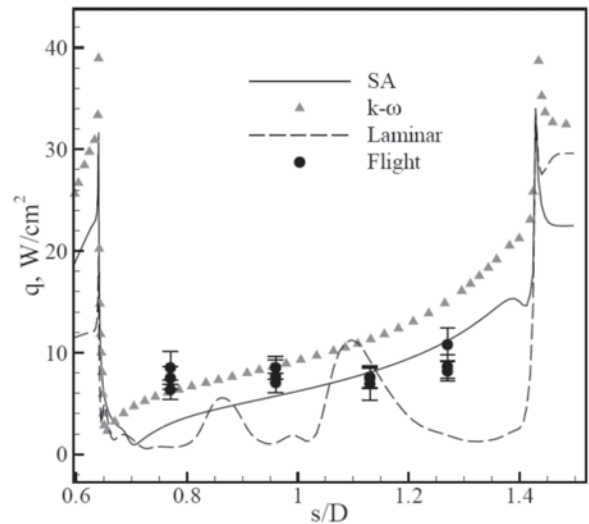


Figure 18. Comparison of computed afterbody heat transfer rate with in-flight measurements⁴¹ for flow over FIRE II capsule at 35 km altitude and Mach 16. (Reprinted with permission of the American Institute of Aeronautics and Astronautics)

- inlet. *In Proceedings of the Symposium on Applied Aerodynamics and Design of Aerospace Vehicle (SAROD-2009)*, Bangaluru, India, 10-12 December 2009. 356-65.
3. Md. Shafeeq Ahmed; Kumar, V.; Sachdeva, A. & Priyadarshi, P. Mono-stability characteristics of re-entry modules CFD studies. *In Proceedings of the Symposium on Applied Aerodynamics and Design of Aerospace Vehicle (SAROD-2009)*, Bangaluru, India, 10-12 December 2009. 288-97.
4. Sivamurugan, T.; Antuvan, D.S. & Sivan, K. Heat flux distribution over forebody of re-entry vehicles. *In Proceedings of the Symposium on Applied Aerodynamics and Design of Aerospace Vehicle (SAROD-2009)*, Bangaluru, India, 10-12 December 2009. pp. 310-23.
5. Asokarajan, N. Hypersonic inviscid flow field analysis for a re-entry crew module. *In Proceedings of the Symposium on Applied Aerodynamics and Design of Aerospace Vehicle (SAROD-2009)*, Bangaluru, India, 10-12 December 2009. pp. 378-93.
6. Sislian, J.P.; Martens, R.P.; Schwartzentruber, T.E. & Parentx, B. Computational aerothermodynamic design issues for hypersonic vehicles. *J. Prop. Power*, 2006, **22**(5), 1039-048.
7. Reddy, D.R. & Weir, L.J. Three-dimensional viscous analysis of a Mach 5 inlet and comparison with experimental data. *J. Prop. Power*, 1992, **8**(2), 432-40.
8. Lanson, F. & Stollery, J.L. Some hypersonic intake studies. *Aeronautical Journal*, 2006, **36**(1), 145-56.
9. Travis, W.; Drayna, Nompelis, I. & Candler, G. V. Hypersonic inward turning inlets: Design and optimisation. *In 44th AIAA Aerospace Sciences Meeting and Exhibit Reno, Nevada, 9-12 January 2006*. 1-11.
10. Wright, M.; Edquist, Karl; Tang, Chun; Hollis, Brian; Krasa, Paul & Campbell, Charles. A review of aerothermal

- modelling for mars entry missions. AIAA Paper-2010-443, 2010.
11. Hollis, B.R.; Berger, K.T.; Horvath, T.J.; Coblisch, J.J.; Norris, J.D.; Lillard, R.P. & Kirk, B.S. Aeroheating testing and predictions for project Orion CEV at turbulent conditions. AIAA Paper-2008-1226, 2008.
 12. Wilcox, D. C. Turbulence modeling for CFD, Ed.3. DCW Industries, 2006.
 13. Spalart, P. R. & Allmaras, S. R. A one-equation turbulence model for aerodynamic flows. AIAA Paper-1992-0439, 1992.
 14. Jones, W.P. & Launder, B.E. The prediction of laminarisation with a two-equation model of turbulence. *Int. J. Heat Mass Trans.*, 1972, **15**(9), 301-14.
 15. Wilcox, D.C. Reassessment of the scale-determining equation for advanced turbulence models. *AIAA Journal*, 1988, **26**(11), 1299-310.
 16. Haidinger, F.A. & Friedrich, R. Computation of shock wave turbulent boundary layer interactions using a two-equation model with compressibility corrections. *In Applied Scientific Research, Advances in Turbulence IV*, edited by F.T.M Nieuwstadt, 1993, **51**(1), 501-505.
 17. Sinha, K.; Mahesh, K. & Candler, G.V. Modelling shock-unsteadiness in shock/turbulence interaction. *Physics Fluids*, 2003, **15**(8), 2290-297.
 18. Veera, V.K. & Sinha, K. Modeling the effect of upstream temperature fluctuations in shock/turbulence interaction. *Physics Fluids*, 2009, **21**(2), 25101-110.
 19. Sinha, K.; Mahesh, K. & Candler, G.V. Modelling the effect of shock-unsteadiness in shock/turbulent boundary layer interactions. *AIAA Journal*, 2005, **43**(3), 586-94.
 20. Pasha, A.A. & Sinha, K. Shock-unsteadiness model applied to oblique shock-wave/turbulent boundary-layer interaction. *Int. J. Comp. Fluid Dyn.*, 2008, **22**(8), 569-82.
 21. Pasha, Amjad Ali & Sinha, Krishnendu. Simulation of three-dimensional shock/boundary-layer interaction in a single-fin configuration. *In 11th Annual AeSI CFD Symposium-2009*, Indian Institute of Sciences, Bangalore, 11-12 August 2009.
 22. Knight, D.; Yan, H.; Panaras, A.G. & Zheltovodov, A. Advances in CFD prediction of shock wave turbulent boundary layer interaction. *Prog. Aero. Sci.*, 2003, **39**(3), 121-84.
 23. Roy, C.J. & Blotter, Fredic G. Review and assessment of turbulent models for hypersonic flows. *Prog. Aero. Sci.*, 2006, **42**(7-8), 469-530.
 24. Wilcox, D.C. Formulation of the k- ϵ turbulence model revisited. *AIAA Journal*, 2008, **46**(11), 2823-838.
 25. Panaras, A.G. Review of the physics of swept-shock/boundary layer interactions. *Prog. Aero. Sci.*, 1996, **32**, 173-244
 26. Alvi, F.S. & Settles, G. Physical model of the swept shock wave/boundary-layer interaction flow field. *AIAA Journal*, 1992, **30**(9), 2252-258.
 27. Reddy, D.S.K. & Sinha, K. Hypersonic turbulent flow simulation of FIRE II re-entry vehicle afterbody. *J. Space Rockets*, 2009, **46**(4), 745-57.
 28. Park, C. Non-equilibrium hypersonic aerothermodynamics. Wiley-Interscience Publication, New York, 1990. pp. 255-68, 326 and 353.
 29. Sarma, G.S.R. Physico-chemical modelling in hypersonic flow simulation. *Prog. Aero. Sci.*, 2000, **36**, 281-49.
 30. Gupta, R.N.; Yos, J.M.; Thompson, R.A. & Lee, K.P. A review of reaction rates and thermodynamic and transport properties for an 11-species air model for chemical and thermal non-equilibrium calculations to 30000 K. NASA Report No. RP-1232, 1990.
 31. Wright, M.J.; Loomis, M. & Papadopoulos, P. Aerothermal analysis of the project FIRE II afterbody flow. *J. Thermophy. Heat Trans.*, 2003, **17**(2), 240-49.
 32. Wilke, C.R. A viscosity equation for gas mixtures. *J. Chem. Phys.*, 1950, **18**, 517-19.
 33. Palmer, G.E. & Wright, M.J. Comparison of methods to compute high-temperature gas viscosity. *J. Thermophy. Heat Trans.*, 2003, **17**(2), 232-39.
 34. Fay, J.A. & Riddell, F.R., Theory of stagnation point heat transfer in dissociated air. *J. Aero. Sci.*, 1958, **25**(2), 73-85.
 35. Reddy, D.S.K. & Sinha, K. Effect of chemical reaction rates on aero-heating predictions of re-entry flows. AIAA Paper-2010-630, 2010.
 36. Bose, D. & Wright, M.J. Uncertainty analysis of laminar aeroheating predictions for Mars entries. AIAA Paper-2005-4682, 2005.
 37. MacCormack, R.W. & Candler, G.V. The solution of the navier-stokes equations using gauss-siedel line relaxation. *Computers Fluids*, 1989, **17**(1), 135-50.
 38. Druguet, M.C.; Candler, G.V. and Nompelis, I. Effect of numerics on Navier-Stokes computations of hypersonic double-cone flows. *AIAA Journal*, 2005, **43**(3), 616-23.
 39. Saunders, D.; Yoon, S. & Wright, M.J. An approach to shock envelope grid tailoring and its effect on re-entry vehicle solutions. AIAA Paper-2007-207, 2007.
 40. Wright, M.J.; Prabhu, D.K. & Martinez, E.R. Analysis of Apollo command module afterbody heating, Part I: AS-202. *J. Thermophy. Heat Trans.*, 2006, **20** (1), 16-30.
 41. Slocumb, T.H. Project FIRE II afterbody temperatures and pressures at 11.35 kilometer per second. NASA Report No. NASA TM X-1319, 1966.

Contributor



Dr Krishnendu Sinha received his BTech (Aerospace Engineering) from the Indian Institute of Technology Kanpur in 1995. He received his Masters and PhD in Aerospace Engineering from the University of Minnesota, USA. He joined Indian Institute of Technology Bombay, Mumbai as Assistant Professor in 2006. Since then, he has focused on the modelling and simulation of high-speed flows. His

research interests and expertise are in the areas of computational fluid dynamics, turbulence modelling and hypersonic flow simulation.